

Flow and Dipole Source Evaluation of a Generic SUV

Accurately predicting both average flow quantities and acoustic sources at the front window of today's ground vehicles are still a considerable challenge to automotive companies worldwide. One of the most important aspects in terms of obtaining not only trustworthy results but also the most tedious one and therefore perhaps overlooked, is the control and outcome of the mesh generation process. Generating unstructured volume meshes suitable for large eddy simulations with high level representation of geometrical details is both a time consuming and an extremely computer demanding activity. This work investigates two different mesh generation processes with its main aim to evaluate their outcome with respect to the prediction of the two dominating dipole sources in a temporal form of the Curle's equation. Only a handful of papers exists that report a high level representation of the vehicle geometry and the aim of predicting the fluctuating exterior noise sources. To the author's knowledge no studies have been conducted in which both these source terms are evaluated quantitatively against measurements. The current paper investigates the degree to which the amplitude of these two source terms can be predicted by using the traditional law-of-the-wall and hex-dominant meshes with isotropic resolution boxes for a detailed ground vehicle geometry. For this purpose, the unstructured segregated commercial FLUENT finite volume method code is used. The flow field is treated as incompressible and the Smagorinsky–Lilly model is used to compute the subgrid stresses. Mean flow quantities are measured with a 14 hole probe for 14 rakes downstream of the side mirror. The dynamic pressure sensors are distributed at 16 different positions over the side window to capture the fluctuating pressure signals. All measurements in this work were conducted at Ford's acoustic wind tunnel in Cologne. All three simulations accurately predict the velocity magnitude closest to the window and downstream of the mirror head recirculation zone. Some variations in the size and shape of this recirculation zone are found between the different meshes, most probably caused by differences in the detachment of the mirror head boundary layer. The Strouhal number of the shortest simulation was computed from the fundamental frequency of the drag force coefficient. The computed Strouhal number agrees well with the corresponding results from similar objects and gives an indication of an acceptable simulation time. The dynamic pressure sensors at 16 different locations at the vehicle side window were also used to capture the levels of the two dipole source terms. These results are compared with the three simulations. With the exception of three positions, at least one of the three simulations accurately captures the levels of both source terms up to about 1000 Hz. The three positions with less agreement as compared with measurements were found to be in regions sensitive to small changes in the local flow direction. [DOI: 10.1115/1.4001340]

Jonas Ask

Department of Environment and Fluid Dynamics
Centre,
Volvo Car Corporation,
SE-405 31 Göteborg, Sweden

Lars Davidson

Professor
Department of Applied Mechanics,
Division of Fluid Dynamics,
Chalmers University of Technology,
SE-412 96 Göteborg, Sweden

1 Introduction

Flow induced noise or wind noise in ground vehicles caused by flow passing the vehicle exterior at cruising speed is undesirable noise as experienced by the driver and passengers. A reduction in and knowledge of the underlying mechanisms of this noise generation and aspiration into the compartment represent a research field of great importance to the world's automotive companies. This flow induced noise can arise from one or several of the following, according to Stapleford and Carr [1]:

- unpitched noise caused by air rushing past the vehicle surface
- monotone noise due to sharp edges and gaps at the vehicle surface
- acoustic resonance caused by flow excitation of vehicle openings such as side windows or sunroofs

This work treats the first item, namely, air rush noise, which has been addressed in wind tunnel measurements and “on road” tests from the mid-1960s until the last decade.

Some examples are given here. In 1964, Thomson [2] conducted road tests to investigate which of the two attributes, aerodynamic shape or seal design, is the most important property in the prevention of wind noise. His study led to the conclusion that the shape of the vehicle is not as important as air leakages caused by poor seal designs. The most critical region in his study was the sealing in the vicinity of the A-pillar, followed by the C-pillar region close to the beltline (see Fig. 1), and the front door region close to the driver or passenger.

A two part study was initiated in 1971 by Stapleford and co-worker [1,3] to associate different flow regimes with aerodynamic noise levels for generic objects and production vehicles. They found that high aerodynamic noise levels were highly associated with different forms of flow separation, particularly from spiral vortex flows. A direct consequence of this finding was that aerodynamic shape is an important factor because minimizing flow separation will help to reduce the wind noise.

Further insight into important parameters for reducing air rush noise was described in Watanabe et al. [4] in 1978. As in Stapleford and co-worker [1,3], they stated that the fundamental cause

Contributed by the Fluids Engineering Division of ASME for publication in the JOURNAL OF FLUIDS ENGINEERING. Manuscript received November 14, 2007; final manuscript received January 18, 2010; published online May 14, 2010. Associate Editor: Rajat Mittal.

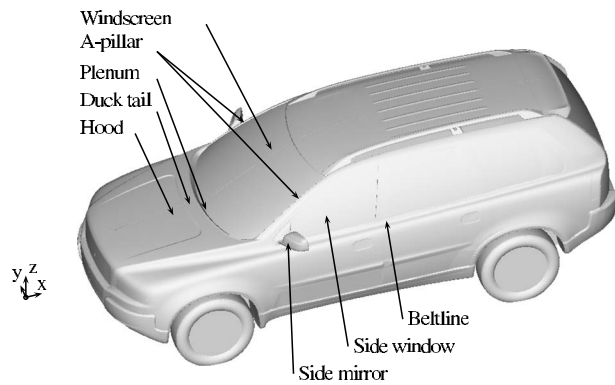


Fig. 1 Vehicle geometry

of air rush noise is flow separation. They also identified the fact that the relationship between the rain gutter height and the side window recess depth is an important parameter in the reduction in noise levels. They wrote that a third way to decrease air rush noise is to reduce local flow velocities. In their work, this was investigated by mounting a wind deflector on the hood, reducing the flow speed at the A-pillar.

The important aspects of aerodynamic noise in ground vehicles were reviewed in 1990 by George [5]. He stated that surface pressure fluctuations caused by flow separations are the most important source of air rush noise. He also presented an approach to tackling the complete aerodynamic noise problem based on the following four steps:

- Understanding the flow field including the separations.
- Finding the surface pressure fluctuations based on this information.
- Finding the external sound radiation from the pressure fluctuations.
- Finally, finding how these pressure fluctuations excite the vehicle structure to generate internal noise.

Numerical attempts to solve these four steps have been made in the last decade and much effort is now directed toward improving and refining existing techniques. The two dominating techniques for predicting separation dynamics as a starting point for wind noise predictions are by the traditional finite volume method (FVM) and the Lattice Boltzmann method (LBM).

Starting with the FVM approach, one of the first papers in which accurate large eddy simulations (LES) of the flow around simplified ground vehicles were made in order to understand the aerodynamics, including flow separation by LES, i.e., point 1, is the work of Krajnović and co-workers [6–9].

Rung et al. [10] conducted a flow and noise radiation study of a generic side mirror in comparisons of unsteady Reynolds averaged Navier–Stokes (URANS) and detached eddy simulations (DES). They compared fluctuating wall pressure and radiated sound computed by the Ffowcs Williams and Hawkins analogy [11] with corresponding measured results. They covered the first three steps in George’s list. Their findings showed a major improvement in the predicted acoustic sources and the radiated sound using the DES model for most surface mounted sensors and microphones as compared with the URANS results.

Posson and Pérot [12] took the geometry complexity one step further by mounting a production mirror on top of a plate and exposing it to a freestream velocity of 40 m/s. Both mean and fluctuating velocity components from the finest resolved case were compared with PIV measurements, showing well predicted trends for all the regions evaluated. Furthermore, fluctuating pressure spectra in the wake were compared with measurements and showed good agreement at one location but underpredicted the decibel levels in the frequency range of 100–1000 Hz at a point

farther downstream. One interesting observation is that two grids of approximately 6×10^6 cells and 5×10^6 cells gave approximately a 10 dB offset in the fluctuating wall pressure spectra.

Several authors [13–15] have also described the use of the LBM approach to estimating aeroacoustic noise sources in flow separated regions. Duncan et al. [13] conducted a simulation past the Ahmed body and used signal processing to visually identify noise sources restricted to different frequency bands.

Senthooran et al. [14] conducted a 0 deg and a 10 deg yaw angle simulation to validate simulated surface pressure spectra over the front side window as compared with measurements for a sedan type vehicle. The probes closest to the beltline and B-pillar showed promising agreement up to about 1000 Hz when compared with the measurements for both yaw angles evaluated.

Gaylard [15] used a similar approach for a full vehicle including side mirrors and rails at a 0 deg yaw angle. His results showed fair predictions of the surface pressure for some of the probes over the side window but an almost 40 dB offset at most at another location.

It appears from the above studies as though the accuracy of the fluctuating surface pressure spectra is dependent more on the location of the dynamic pressure sensors in relation to the local flow than on the methodology used. In other words, the dynamic pressure sensors located in regions with high spatial gradients of the source rms levels are more likely to deviate as compared with sensors located in a more diffuse region.

The third step in George’s list has partly been covered by some of the above mentioned authors but is further discussed here. The most straightforward way is to compute the sound radiation directly. With this approach it is possible to evaluate sound emissions at any point within the computational domain. This technique however puts enormous constraints on both numerical schemes and boundary conditions in order to capture the wide range of scales present in any turbulent flow field. If the interest instead is in finding the emissions at points outside the computational domain or from an incompressible flow field, a different strategy must be used. For flows where walls are present, a feasible method is to use either the analogy of Ffowcs Williams and Hawking [11] or the analogy of Curle [16]. These analogies convert the governing momentum and continuity equations to an inhomogeneous wave equation. Studies of the incompressible assumption combined with a time formulation of Curle’s analogy were reported in Ask and Davidson [17,18]. Discrepancies in the sound directivity were caused by a phase mismatch of the sources in the incompressible flow as compared with the compressible flow cause by a sudden change in the geometry. The main conclusion of their work was that the incompressible treatment, even at a Mach number of ($Ma < 0.15$), can be unsuitable when predicting sound radiation based on acoustic analogies since the flow has no possibility to expand or compress. Even though this compression/expansion of the flow is small compared with the gross characteristics of the flow, the radiated sound will be a consequence of a more or less complete cancellation of large source regions, which amplifies subtle details of the flow. Even at low Mach number, a compressible treatment of the flow is therefore more appropriate for flows, for example over, cavities, rear, and forward facing steps, where the flow takes a sudden change in direction. However, the incompressible flow field could accurately predict the levels of the two dominating dipole source terms. This was the chief motivation for the present work, where both flow and geometrical complexity are significantly increased. The time formulation of Curle’s analogy, Eq. (1), uses the temporal derivatives inside the integral instead of keeping the spatial derivatives outside the integral, as Curle’s [16] original formulation states.

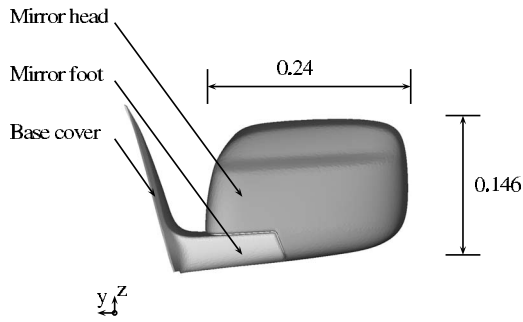


Fig. 2 Mirror geometry, front view

$$p(\mathbf{x}, t) - p_\infty = \frac{1}{4\pi} \int_V \left[\frac{l_i l_j}{a_\infty^2 r} \ddot{T}_{ij} + \frac{3l_i l_j - \delta_{ij}}{a_\infty r^2} \dot{T}_{ij} + \frac{3l_i l_j - \delta_{ij}}{r^3} T_{ij} \right] dV(\mathbf{y}) + \frac{1}{4\pi} \int_S l_i n_j \left[\frac{\dot{p} \delta_{ij} - \dot{\tau}_{ij}}{a_\infty r} + \frac{p \delta_{ij} - \tau_{ij}}{r^2} \right] dS(\mathbf{y}) \quad (1)$$

In Eq. (1), the acoustic pressure fluctuation at an observer located at \mathbf{x} is evaluated from a forward time projection of two integrals evaluated at the source location \mathbf{y} . The first integral contains the volume contribution, where $T_{ij} = \rho u_i u_j - \tau_{ij} + (p - a_\infty^2 \rho) \delta_{ij}$ is commonly referred to as the Lighthill tensor. The dot(s) above T_{ij} , τ_{ij} , and p denote time derivative(s) and l_j is the unit vector pointing from the source to the observer; the terms in this integral are often referred to as quadrupole terms. The second integral contains the surface integral and consists mainly of the fluctuating pressure and the fluctuating pressure temporal derivative. These terms are commonly referred to as dipole terms and are often regarded as the dominating terms for low Mach number wall bounded flows. The derivation of the expression above can be found in Ref. [19].

The text is organized in the following way. The Sec. 2 describes the object. This is followed by a description of the methodology used for the different simulations and a brief description of the measurement techniques (Sec. 3). The flow field results are given in Sec. 4 followed by the acoustic source results (Sec. 5). Section 6 concludes the results and is followed by the acknowledgment.

2 Case Description

The object in the present study is a side mirror mounted on a simplified sport utility vehicle. Both the underbody and wheel geometry are simplified as compared with a production vehicle due to their low impact on the flow above the beltline. The vehicle geometry at the present state is shown in Fig. 1 together with the identification of different parts used in the text.

Some parts in Fig. 1 are self explanatory, such as the front and side windows, the side mirror, and the hood but the remaining parts require additional description. The A-pillar is the roof support structure separating the front and side windows. The duck tail is an elevation of the rearmost part of the hood that has the purpose of screening the washer nozzles and wipers both visually and aerodynamically. The plenum is the space between the rearmost

part of the hood and the windscreen and, finally, the beltline refers to the topmost horizontal line of the vehicle before reaching the glazed-in greenhouse region. A close-up of the mirror geometry is shown in Fig. 2. The mirror head width and height are 0.24 m and 0.146 m, respectively, and the projected area including both head and foot is 0.034 m². The Reynolds number based on the mirror height is $Re_H \approx 3.8 \times 10^5$. In the following text, the mirror head refers to the darker part in this figure and the mirror foot is the support structure between the vehicle exterior and the mirror head, here identified as the lighter of the two.

The coordinate system is defined as follows: the x -axis follows the streamwise direction, the y -axis originates at the vehicle symmetry plane and is directed out of the domain, and the z -axis is normal to the ground surface.

3 Methodology

Two mesh generation processes are investigated and will be explained briefly here. In the first process, ICEM 5.1 grid generator is used to generate the volume mesh. Resolution boxes are here used for increased resolution in the investigated regions. In the first step of this process, an isotropic grid is generated with a Cartesian cell structure. Each Cartesian cell is built of 12 tetrahedral cells and is restricted to the off-wall region. This is also the main drawback of the present approach due to an initial mesh determined by the memory size of the front-end computer. In the second step, two prism layers are generated closest to the solid walls; in the final step, the grouped 12 tetrahedral cells are converted into one hexahedral cell if the quality restriction for the hexahedral cells is kept. This process took about 30 h (man time and CPU time) for each case on a double processor 32 GB HPC8000 computer but gives the user full control of both the mesh quality and the near-wall resolution.

In the second process, HARPOON 2.4 is used with resolution boxes similar to those in the ICEM process. The advantage of this code is first that the algorithm skips the mesh subdivision and generates a hexahedral dominant mesh directly and second that the whole mesh process took slightly more than 1 h (man time and CPU time). A drawback of this approach is that the prism generation is not sufficiently stable for this version and is therefore in this work partly compensated for by both a slower cell growing ratio close to the wall and a higher resolution.

Three different grids were investigated based on the above processes, two with ICEM and one mesh based on the HARPOON process. The two ICEM meshes are called GSM1I and GSM2I with grid sizes corresponding to 6.6×10^6 cell and 8×10^6 cells, respectively. The third grid based on the HARPOON mesh is called GSM3H and consists of 19.6×10^6 cells. The three cases are summarized in Table 1.

The first column in Table 1 gives the case identifications used in the following text. The second column gives the number of prism layers in the different cases. The third and fourth columns show the maximum cell size for the two most important resolution boxes. The fifth column gives the average n^+ over the A-pillar, mirror foot, and the mirror head, where n^+ refers to the wall normal direction. The final column gives the average number of cells

Table 1 Description of the three meshes

Grid definitions					
ID	No. of prism layers	Cell size mirror wake (mm)	Cell size A-pillar region (mm)	Avg. n^+ A-pillar/mirror foot/mirror head	No. of cells resolving the mirror sail log-layer
GSM1I	2	4	8	50/72/70	6
GSM2I	2	4	4	53/70/70	6
GSM3H	0	2.5	2.5	40/111/102	5

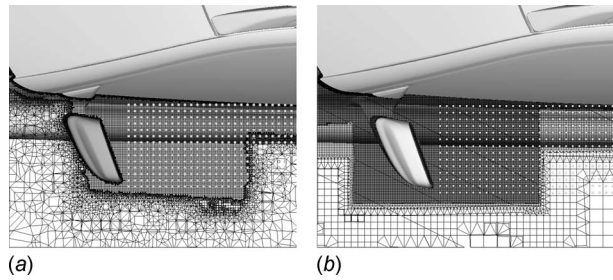


Fig. 3 Mesh cut planes for GSM2I and GSM3H: (a) cut through the mesh of case GSM2I and (b) cut through the mesh of case GSM3H

used for resolving the mirror sail log-layer ($n^+ < 500$). A cut-plane of the mesh is shown in Figs. 3(a) and 3(b) for cases GSM2I and GSM3H, respectively. The code used in this paper is the FLUENT 6.2.16 unstructured solver. It is based on a control volume formulation to convert the governing equations to a solvable algebraic set of equations. The code uses a collocated scheme with cell-centered storage of both scalars and vectors. The freestream velocity for the current simulation is 39 m/s, resulting in an ambient Mach number of 0.11, which implies that the incompressible assumption is justified. The bounding domain extends from the inlet located 20 m upstream of the front bumper to the outlet located 24.8 m downstream of the rear bumper. The farfield boundaries are located 9 m above the ground and 4.7 m from the symmetry plane. The vehicle is symmetric about the $y=0$ plane and, thus, only half the geometry is computed. The symmetry boundary condition is generally not recommended for LES due to its physical restriction for the three dimensionality of turbulent structures. However, the aim of the present work is to study the separated flow downstream of the A-pillar and side mirror, which is believed to have a small impact on the boundary condition at $y=0$.

The spatial discretization scheme used in the present work is a bounded central differencing scheme, which is essentially a second-order central scheme with a wiggle detector for wavelengths of $2\Delta x$ or less. For these occasions it blends to a second-order upwind scheme or, in the worst case, a first-order upwind scheme. The discretization in time follows an implicit second-order scheme, and at least five subiterations were conducted for each time step. The subgrid-scale stresses are computed by the Smagorinsky–Lilly model, where the eddy viscosity is modeled as

$$\nu_t = \rho L_s^2 |\bar{S}| \quad (2)$$

where S is the magnitude of the strain-rate tensor and L_s is the mixing length for subgrid scales and is defined as

$$L_s = \min(\kappa d, C_s V^{1/3}) \quad (3)$$

In Eq. (3), κ is the von Karman constant, d is the distance to the closest wall, C_s is the Smagorinsky constant, and V is the cell volume. In the present work, $C_s=0.1$. At solid boundaries, the log-law is applied for cells located in the range of $30 < n^+ < 300$, and a linear velocity relation is assumed for cells located at $n^+ < 5$. A blending of the wall shear stress is carried out in the intermediate region. The freestream velocity is applied at the inlet. Other boundary conditions used in the present work are a pressure boundary condition at the outlet and symmetry conditions at the farfield boundaries. The ground surface is modeled as a wall boundary and moves at the same speed as the freestream velocity.

The following simulation procedure was used. After a total simulation time of $160H/U$, an extraction of statistics and wall pressures was initiated and case GSMII was run for a further $160H/U$. Here, H is the mirror head maximum height, see Fig. 2, and U is the freestream velocity. An interpolated solution field was then created as an initial solution for the other two cases.

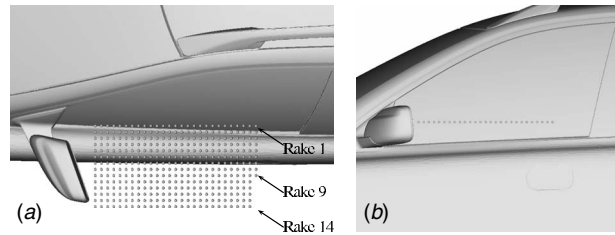


Fig. 4 Positions of the 14 hole probe: (a) probe location, top view and (b) probe location, side view

Case GSM2I was run from this solution for a further $53H/U$ before initiating extraction of the statistics. The simulation was then run for a further $160H/U$. GSM3H was initiated from the same solution as GSM2I and was run $77H/U$ before extracting statistics. After a total simulation time of $184H/U$, this final simulation was terminated. The time step for all cases was $\Delta t = 2 \times 10^{-5}$ s.

The flow measurements downstream of the side mirror were made by Ford Merkenich through scans at discrete points with a T-shaped 14 hole probe at their acoustic wind tunnel. The streamwise length of the probe is 14 mm and it has a cross-flow diameter of 4 mm; the locations of these points are shown in Fig. 4. The distance from the innermost rake to the side window varies between 25 mm at the farthest upstream point to 3 mm for the point located farthest downstream. A grid spacing of 20 mm in both the streamwise and spanwise directions was used for these measurements. The measurements of the mirror wake are grouped into 14 streamwise rakes, where the first rake is located closest to the window and the last rake is the most distant measured from the $y=0$ plane.

The two acoustic source terms evaluated in this work are

$$P_w^{\text{rms}} \frac{\dot{P}_w^{\text{rms}}}{a_\infty} \quad (4)$$

where the first refers to source term 1 and the second refers to source term 2, see Eq. (1). In Eq. (4), the dot represents a time derivative and $a_\infty = 343$ m/s. The dynamic surface pressure was measured through ten integrated circuit piezoelectric type 103B01 acoustic pressure sensors from PCB Piezotronics Inc., mounted on the inside of a 5 mm thick polycarbonate window by an adhesive mounting ring. A 3.0 mm hole through the window connected the microphone with the external flow. The dynamic pressure was measured in two sequences to obtain a total of 16 measurement points. These locations are shown in Fig. 5. The fluctuating pressure sequence was then used to reconstruct the second source term.

4 Flow Field Results

Freestream air is accelerated above the hood starting from the grille stagnation line, see Fig. 1. The duck tail close to the rear edge of the hood affects the flow by lifting the windscreen stag-

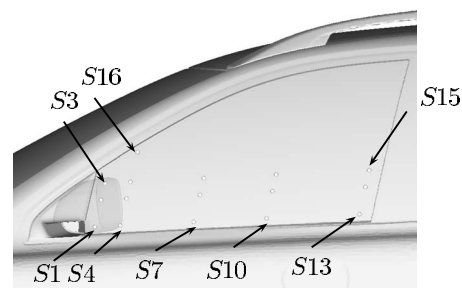


Fig. 5 Positions of the dynamic pressure sensors

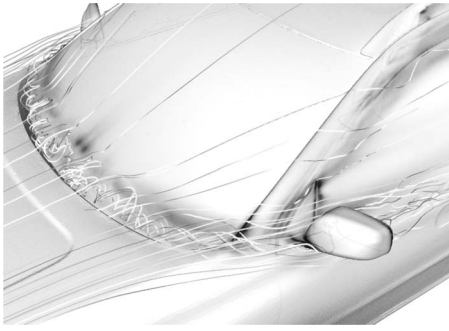


Fig. 6 Flow field for case GSM2I. Contours denote p_{rms} . Black corresponds to high values (150 Pa) and white is $p_{rms}=0$.

nation line. This stagnation line divides the flow into one vortical structure within the plenum excited by flow passing above the plenum and a boundary layer flow at the hood directed toward the roof and the A-pillar, Fig. 6. Depending on the shape and angle of the A-pillar, the flow passing the A-pillar can be more or less well controlled. The A-pillar angle and radius also determine the shape

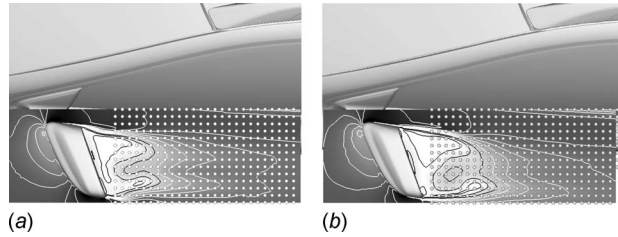


Fig. 7 Velocity magnitude for cases GSM3H and GSM2I: (a) velocity magnitude for case GSM3H and (b) velocity magnitude for case GSM2I

and strength of the spiral vortex at the front door frame. At the lower part of the A-pillar, the flow separates due to the adverse pressure gradient and is directed either below or above the mirror foot, see Fig. 2. Between the base cover and the inner side of the mirror head, the flow is initially accelerated as a result of the converging flow path.

Downstream of this point, the flow decelerates and separates at the downstream part of the base cover, causing high levels of

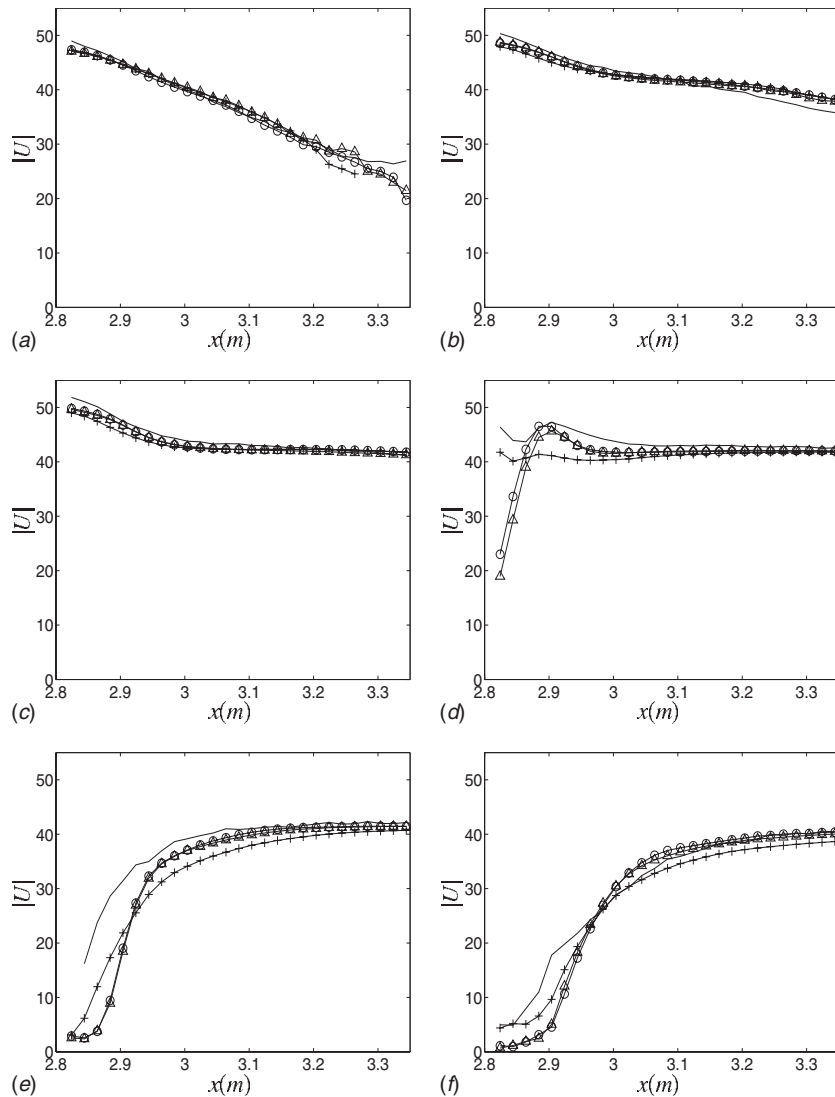


Fig. 8 $|U|$ along rakes 1–6, GSM11 (Δ), GSM2I (\circ), and, GSM3H ($+$) measured (—): (a) $|U|$ along rake 1, (b) $|U|$ along rake 2, (c) $|U|$ along rake 3, (d) $|U|$ along rake 4, (e) $|U|$ along rake 5, and, (f) $|U|$ along rake 6

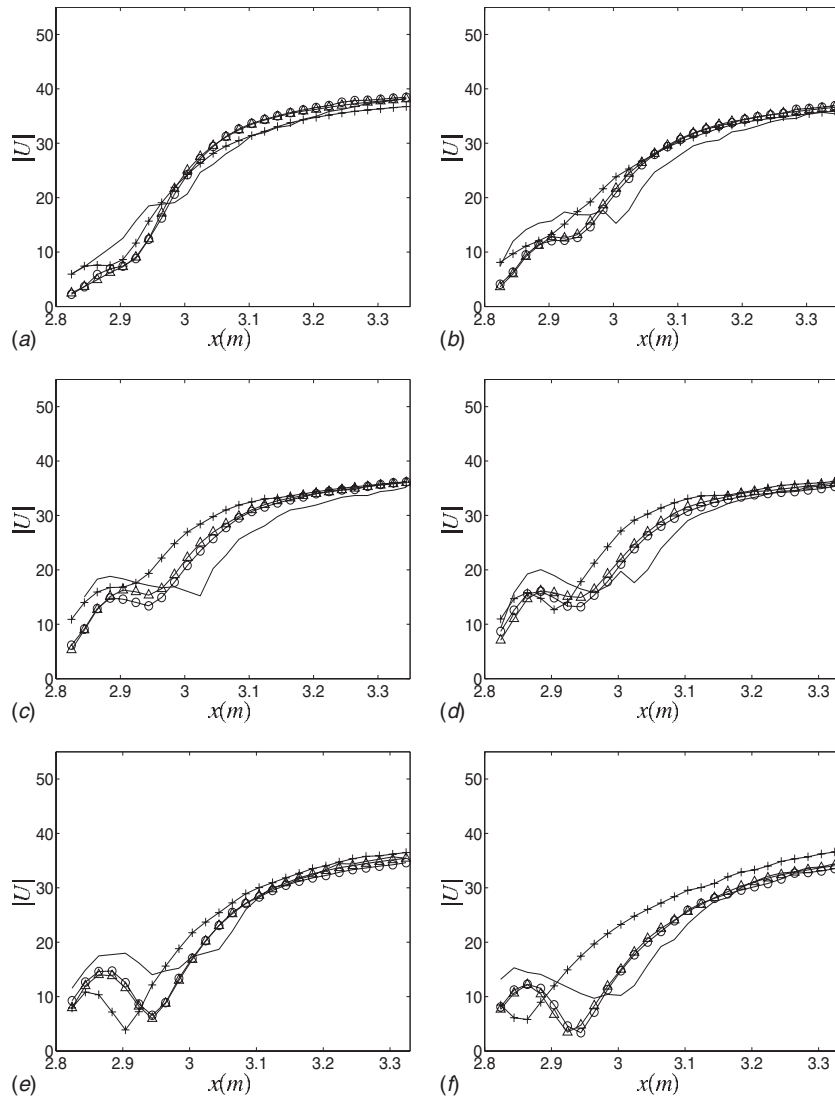


Fig. 9 $|U|$ along raked 7–12, GSM1I (Δ), GSM2I (\circ), and GSM3H (+) measured (–): (a) $|U|$ along rake 7, (b) $|U|$ along rake 8, (c) $|U|$ along rake 9, (d) $|U|$ along rake 10, (e) $|U|$ along rake 11, and, (f) $|U|$ along rake 12

pressure fluctuations at the foremost part of the front side window. The vortex within the plenum is ejected at the junction between the plenum, the hood and the A-pillar root. Depending on the position and shape of the side mirror, this flow is either directed

beneath the mirror foot, which is the case in the present work, or can be directed above the foot. This is the general description of the flow past the A-pillar and the side mirror region; below follows a comparison of the flow in the mirror wake.

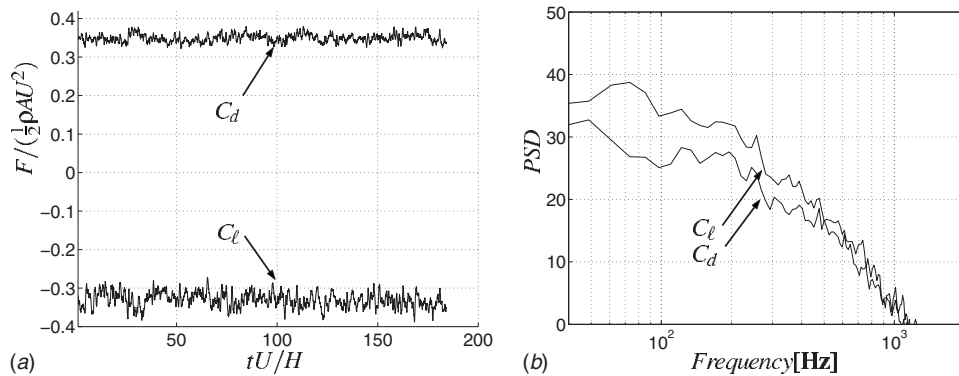


Fig. 10 C_d and C_l for GSM3H: (a) mirror streamwise and floor normal force coefficient and (b) PSD of the force coefficients

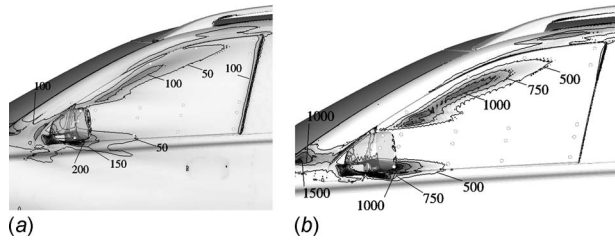


Fig. 11 Contours of the two dipole source terms: (a) contours of source term 1 and (b) contours of source term 2

Figure 7 compares the mean velocity magnitude at the plane at which the 14 hole probe measurements were made.

For the inner rake adjacent to the window, Fig. 8(a), the distance to the window decreases with an increased streamwise position. This is also reflected in the mean velocity magnitude, which decreases slowly along the rake. For the last four points in this rake, a more rapid decay of the velocity magnitude can be seen for all the simulations, which is explained by the proximity of the

window. Again, the last point is located only 3 mm from the window. The measurements break this trend where the velocity magnitude is seen to level out and even increases for the point located farthest downstream in this rake. It appears here as though the probe induces an increased flow speed by blocking the near-wall flow and thus inducing a higher outer flow speed. For rakes 2 and 3, Figs. 8(b) and 8(c), the velocity magnitude shows good agreement between the three simulations and the measurements. A jetlike flow is created between the mirror head and A-pillar with a direction determined mainly by the angle of the mirror head. The presence of this jet is indicated in the points located farthest upstream in rake 2 but is more pronounced for rake 3. Rake 4 shows a slightly different result than the first three rakes, where case GSM3H seems to catch the trend even though the levels are too low for the upstream part of this rake. One way to interpret this result is that the flow has separated from the inner side of the mirror head in both the measured flow field and in case GSM3H, as is indicated in Fig. 7(a). This gives a slightly narrower wake as compared with cases GSM1I and GSM2I, where an attached flow leaves the mirror trailing edge. The streamwise velocity gradients identified in these two cases are therefore caused by the shear

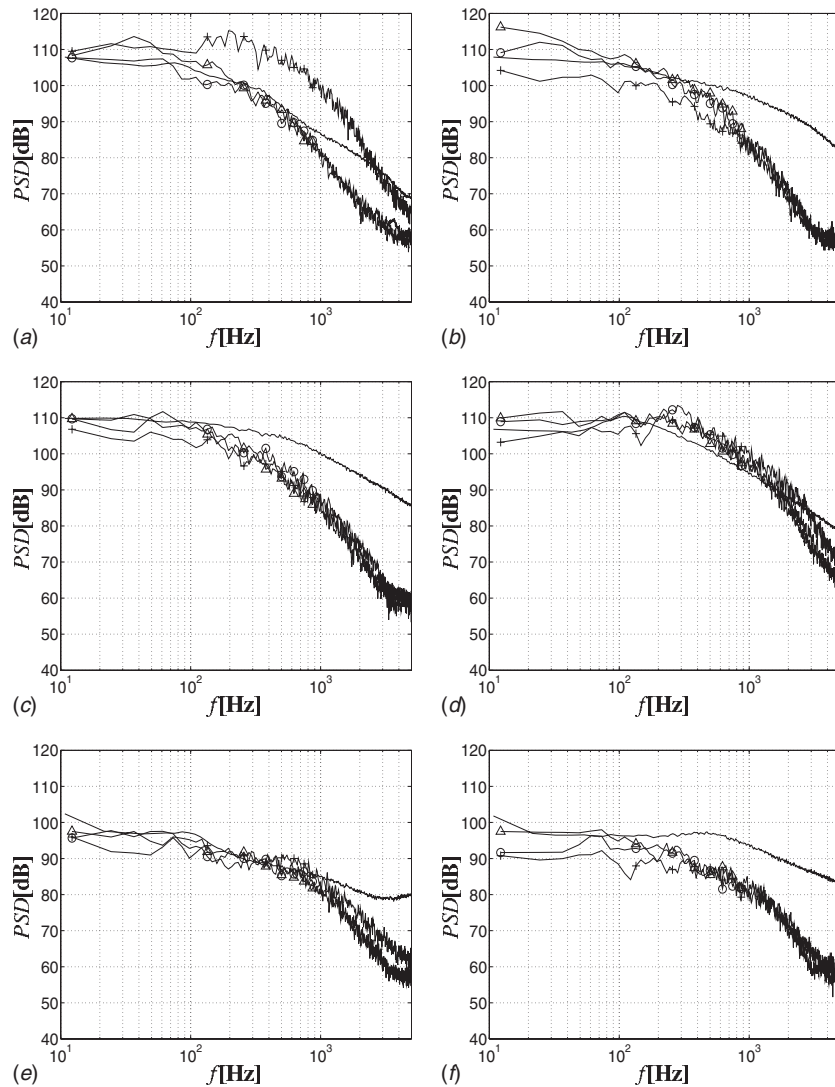


Fig. 12 Power spectral density of source term 1 for cases GSM1I (Δ), GSM2I (\circ), and, GSM3H ($+$) measured ($-$), where $p_{ref}=2e^{-5}$ Pa: (a) PSD of source term 1 at position 1, (b) PSD of source term 1 at position 2, (c) PSD of source term 1 at position 3, (d) PSD of source term 1 at position 4, (e) PSD of source term 1 at position 5, and, (f) PSD of source term 1 at position 6

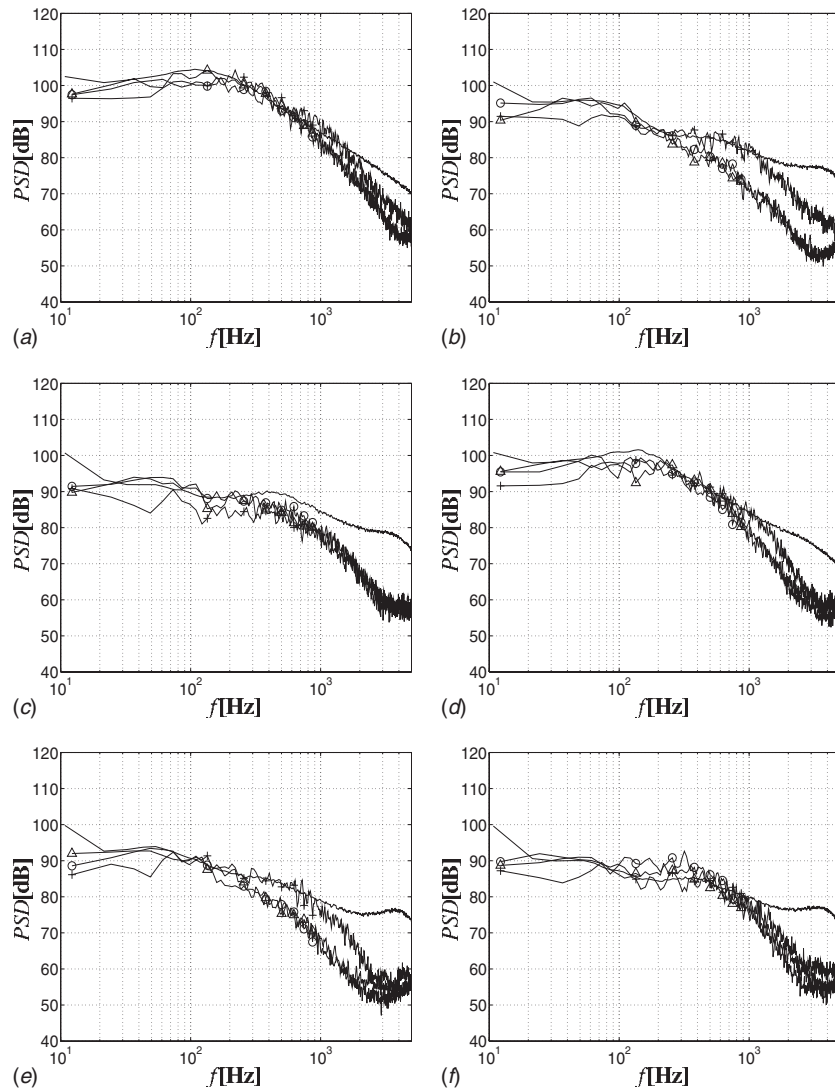


Fig. 13 Power spectral density of source term 1 for cases GSM1I (Δ), GSM2I (\circ), and, GSM3H ($+$) measured ($-$), where $p_{\text{ref}}=2e^{-5}$ Pa: (a) PSD of source term 1 at position 7, (b) PSD of source term 1 at position 8, (c) PSD of source term 1 at position 9, (d) PSD of source term 1 at position 10, (e) PSD of source term 1 at position 11, and (f) PSD of source term 1 at position 12

layer, which is located closer to the side window compared with case GSH3H. In rake 5 the farthest upstream point is located in the mirror wake and the next point along the rake cuts through the shear layer. Judging from Fig. 8(e) it appears as though all simulations overpredict the streamwise extent of the mirror recirculation zone but a small difference in the spanwise location of the shear layer can very well cause this effect. In the final rake in this series, Fig. 8(f), the agreement between the simulations and measurements is again better. The 14 hole probe gives smooth and continuous profiles up to rake 4 when traversed downstream but shows a tendency from rake 5 and higher to give a shaky profile, for example, for rake 6, point 5.

In Fig. 9(a), case GSM3H agrees well with the measured results and a small underprediction of the velocity magnitude can be seen for the other two simulations in the upstream part of the mirror wake. Rake 8, Fig. 9(b), starts in the recirculation zone in the mirror wake where the velocity magnitude slowly increases downstream. At point 6 in this rake, the maximum level is found in the case of the measurements while the corresponding peak is found for point 5 in cases GSM1I and GSM2I. The level decreases

downstream of this peak until the end of the recirculation zone is reached, where the level again increases. Figure 9(c) shows the rake located approximately in the center of the mirror and, from this rake to the end, i.e., rake 14, cases GSM1I and GSM2I show slightly better agreement with the measurements than case GSM3H. The recirculation zone in the upstream part of rake 3 is both more distinguished and located farther upstream as compared with rake 8. Even though case GSM3H has the highest resolution in the mirror wake region, the results deviate to a greater extent with higher rake number as compared with the other two simulations. One possible explanation is the insufficient near-wall resolution.

The mean streamwise force coefficient of the mirror is as follows: $\bar{C}_{d,\text{GSM1I}}=0.3624$, $\bar{C}_{d,\text{GSM2I}}=0.3648$ and $\bar{C}_{d,\text{GSM3H}}=0.349$. The lift force coefficient was also extracted for case GSM3H for which the time sequences of the two force components are presented in Fig. 10(a). To determine the fundamental frequency of the mirror, the power spectral density (PSD) was computed for both components, Fig. 10(b).

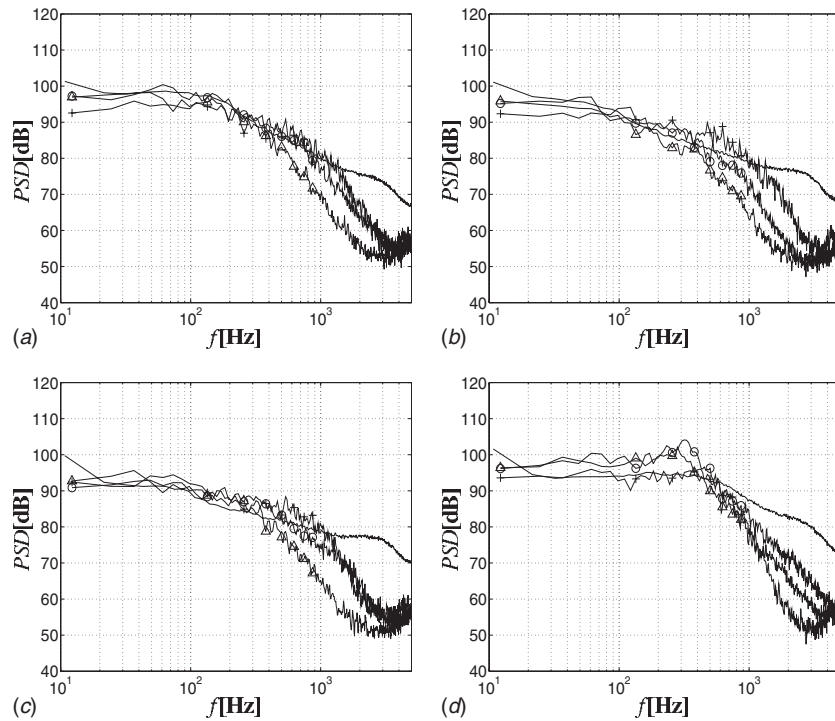


Fig. 14 Power spectral density of source term 1 for cases GSM1I (Δ), GSM2I (\circ), and GSM3H ($+$) measured ($-$), where $\rho_{\text{ref}}=2e^{-5}$ Pa: (a) PSD of source term 1 at position 13, (b) PSD of source term 1 at position 14, (c) PSD of source term 1 at position 15, and (d) PSD of source term 1 at position 16

The peak levels from Fig. 10(b) were found at $f_n(\text{lift})=73$ Hz and $f_n(\text{drag})=49$ Hz, which determined the fundamental frequency. The Strouhal number could then be computed according to

$$\text{St} = \frac{f_n(\text{drag})H}{U_\infty} \quad (5)$$

In Eq. (5), St is the Strouhal number, H is the mirror head height and U_∞ is the freestream velocity. The Strouhal number was then computed to be $\text{St}=0.18$, which is close to other bluff body objects, such as cylinders and spheres. This means that one period is covered within $4.37H/U$ and the shortest simulation, GSM3H, contains approximately 24 periods of this frequency.

5 Acoustic Results

Figure 11 shows contours of the two source terms investigated (see Eqs. (1) and (4)) together with the location of the dynamic pressure sensors (shown in Fig. 5). Figure 11(a) shows the rms level of source term 1 at the front part of the greenhouse. The effect of the A-pillar vortex is clearly marked in this figure by a thin region close to the door frame. Still, the highest level of this source term is found at the lee side of the lower part of the mirror foot caused by the sudden change in the geometry of the mirror foot combined with high local velocities for this region. Source term 2 represents the temporal variation in the first term. This means that the highest levels will be found in regions with short time scales. Figure 11(b) shows a high correlation with source term 1 but it must be kept in mind for this term that the two terms cannot be compared quantitatively as they represent sources to Curle's equation with different dependencies with respect to the distance to an observer (r and r^2 , respectively, see Eq. (1)). However, both terms show maximum levels in the vicinity of the mirror foot and the second highest levels at the root of the A-pillar. The two pictures can also give a hint of the difficulties associated with the comparison of different data sets for a coarse measure-

ment grid, as in the present case. A small shift in the location of the present unsteady structures will have a great effect on the PSD spectra because of the sharp gradient that exists, for example, at the sensors located closest to the base cover.

Position 1, Fig. 12(a), is located at the lee side of the mirror foot. Cases GSM1I and GSM2I agree well with measured levels up to about 1000 Hz, and case GSM3H shows a clear overprediction for the whole resolved frequency range for this position. The reason is primarily that, in this case, the shear layer is directed slightly more downward when leaving the trailing edge of the mirror foot as compared with the other two cases. In addition, the flow stays attached for a greater distance downstream of the junction between the mirror foot and the base cover. This has the effect of directing the flow to the window in this case, generating high fluctuation levels. At position 2, Fig. 12(b), the flow separates smoothly from the trailing edge of the base cover, similar to the flow at position 1 in cases GSM1I and GSM2I. All simulations predict this up to 300 Hz, where the levels decay rapidly as compared with the measured signal. The resolution here is apparently insufficient to capture the turbulent structures. Comparing the measured results at positions 1 and 2, there are significantly higher levels for the intermediate frequencies at the latter position. At position 3, Fig. 12(c), the flow follows the curvature of the base cover trailing edge and again directs the flow toward the window in all simulations. The measured level increases also at this point in the intermediate frequency range, and the simulations have clear problems predicting these levels accurately.

The findings thus far in the most upstream part of the window are mainly determined by the flow passing between the mirror house and the base cover. The variation in the position that captures the unsteady dynamics of this region primarily affects the frequency range between 100 Hz and 5000 Hz, judging from the measurements. The next three points are positioned further downstream at the side window. The measurements at position 4, Fig. 12(d), indicate a small peak at 100 Hz while GSM2I indicates a peak close to 250 Hz. The other two cases exhibit a more broad-

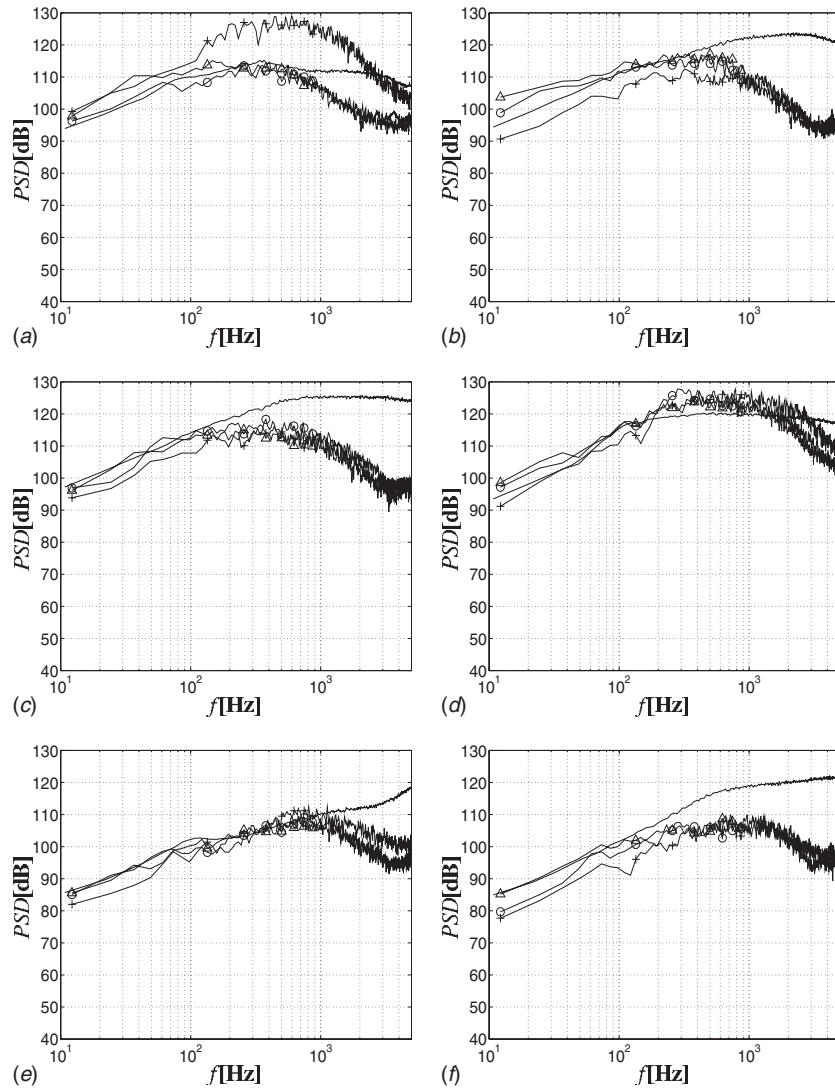


Fig. 15 Power spectral density of source term 2 for cases GSM1I (Δ), GSM2I (\circ), and GSM3H (+) measured (—), where $\rho_{\text{ref}}=2e^{-5}$ Pa: (a) PSD of source term 2 at position 1, (b) PSD of source term 2 at position 2, (c) PSD of source term 2 at position 3, (d) PSD of source term 2 at position 4, (e) PSD of source term 2 at position 5, and (f) PSD of source term 2 at position 6

banded character, and, except for the peak, all simulations follow the measurements up to about 2000 Hz. The peak is caused by vortex shedding downstream of the mirror and leaves a rather broad footprint in Fig. 11(a). The levels are significantly reduced at position 5 as compared with the first four positions because of a more steady flow field. The levels here are well predicted up to about 1000 Hz in all the cases, Fig. 12(e). For position 6, Fig. 12(f), a flat level can be seen all the way up to 600 Hz in the measurements. The three simulations capture this trend up to about 300 Hz, where the decay starts and they rapidly begin to lose energy. The spiral A-pillar vortex is located between positions 6 and 16, Fig. 14(d), and the measured results of these two points are fairly similar.

For position 7, Fig. 13(a), the agreement in levels for the measured results and for case GSM3H matches up to almost 2000 Hz. This position and downstream of position 15 are characterized by a smaller spatial gradient of source term 1. This is also reflected in the results with a generally higher correlation between measured and simulated results. The resolution zone has ended in case GSM1I for the last positions at the lower part of the window, and the effect is clearly reflected in Figs. 14(a)–14(c) with a much

earlier decay in source levels. The last result for source term 1 is shown for position 16, located closer to the door frame than the other points, Fig. 14(d). The only case with a sufficient grid resolution in this region is GSM3H, which predicts the measured frequencies perfectly up to about 700 Hz.

Source term 2 is somewhat more difficult to analyze than the first source term because of its more abstract interpretation. This source increases with short time scales, however, and is comparatively smaller for the more slowly varying flow structures even if the magnitude of their fluctuation is large. This is typically the case for the subsequent results at the same positions, as previously investigated for source term 1. Here the level increases with increased frequency instead of the opposite. There is of course an upper limit at which dissipation takes place but that maximum is not always present in the results or at least not in the frequency range investigated. Even though the physical interpretation of source term 2 is different than that of source term 1, the trends are still very similar to what was found in the previous text. For example, at position 1, Fig. 15(a), the levels in case GSM3H were significantly overpredicted due to a mismatch of the upstream flow field. The other two cases, GSM1I and GSM2I, accurately

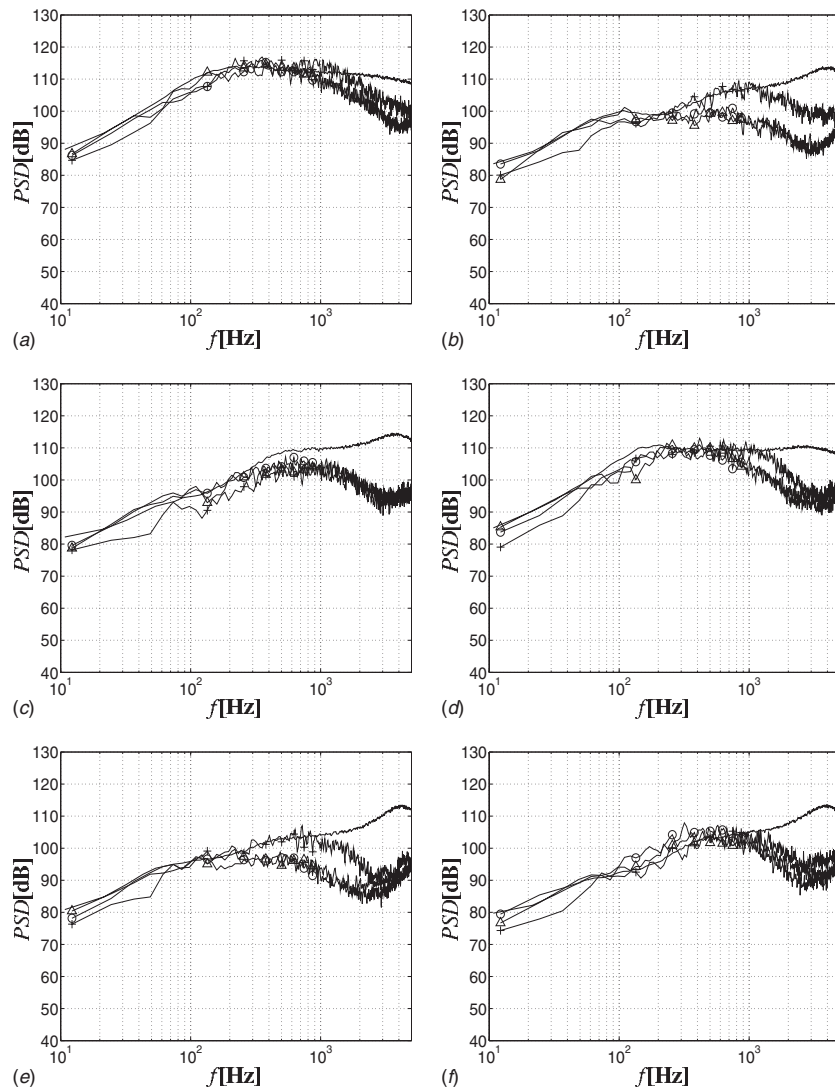


Fig. 16 Power spectral density of source term 2 for cases GSM1I (Δ), GSM2I (\circ), and GSM3H ($+$) measured ($-$), where $\rho_{\text{ref}}=2e^{-5}$ Pa: (a) PSD of source term 2 at position 7, (b) PSD of source term 2 at position 8, (c) PSD of source term 2 at position 9, (d) PSD of source term 2 at position 10, (e) PSD of source term 2 at position 11, and (f) PSD of source term 2 at position 12

predicted the levels up to about 1000 Hz, and similar results are found for this source term. One striking thing about the results is that it appears as though the numerical cut-off is much more pronounced in these results than in the results for source term 1. Of all the positions investigated, the highest levels measured are found at position 3, followed by position 2. This is interesting because it shows the importance and potential of better aerodynamic design of this region of the vehicle, see Figs. 16 and 17. As mentioned in the text above, the flow in this region is extremely complex and involves several geometrical parameters. Except for positions 2, 3, and 6, the results are seen to be very well predicted in at least one of the three cases.

6 Conclusion

This paper reports an investigation of the degree to which the amplitude of the two dominating dipole source terms in Curle's equation can be predicted by using the traditional law-of-the-wall and hex-dominant meshes with isotropic resolution boxes for a detailed ground vehicle geometry.

Three simulations were made using the Smagorinsky-Lilly model combined with the law-of-the-wall for the near-wall region.

Two different mesh strategies were investigated, both with hex-dominant meshes and with the use of local resolution boxes. Two different meshes were investigated in the first process with different resolution zones and employing two prism layers at the solid walls. The second strategy contains no prism layers but these are partly compensated for by higher resolution. Although the size mesh of the GSM3H is three times more than two other cases (GSM1I and GSM2I) there is no significant change in results to be seen. The main reason is probably the prism layer, which is used for cases GSM1I and GSM2I but not for case GSM3H.

The flow field results containing the velocity magnitude are compared for the three simulations and the 14 hole probe measurement made at the acoustic wind tunnel in Ford Merkenich at 14 rakes located in the mirror wake. Closest to the window and downstream of the mirror head recirculation zone, all three simulations accurately predict the velocity magnitude. Some variation in the size and shape of this recirculation zone is found between the different meshes, most probably caused by differences in the detachment of the mirror head boundary layer.

The Strouhal number of the shortest simulation case, GSM3H, was computed from the fundamental frequency of the ground nor-

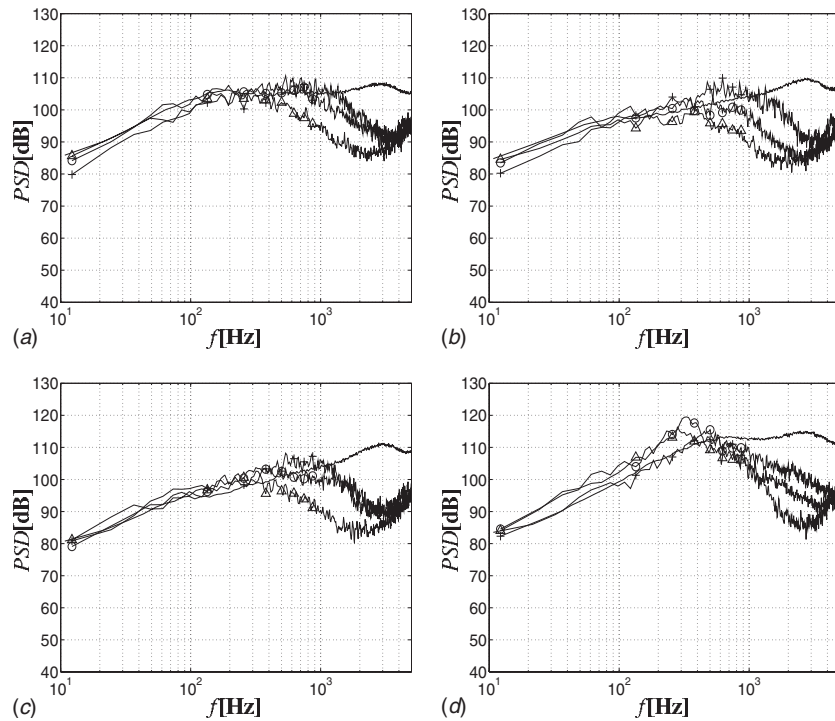


Fig. 17 Power spectral density of source term 2 for cases GSM11 (Δ), GSM21 (\circ), and GSM3H (+) measured (—), where $\rho_{ref}=2e^{-5}$ Pa: (a) PSD of source term 2 at position 13, (b) PSD of source term 2 at position 14, (c) PSD of source term 2 at position 15, and (d) PSD of source term 2 at position 16

mal force component. The computed Strouhal frequency agrees well with the flow past similar objects and gives indications of an acceptable simulation time.

In addition, dynamic pressure sensors at 16 different locations at the vehicle side window were used to capture the levels of the two dipole source terms. These results are compared with the three simulations. Except for at three positions, at least one of the three simulations accurately captures the levels of both source terms up to about 1000 Hz. The three positions with poorer agreement with measurements were found in regions sensitive to small changes in the local flow direction.

Acknowledgment

This work was supported by the Volvo Car Corporation and the Swedish Agency for Innovation Systems (VINNOVA).

References

- [1] Stapleford, W., and Carr, G., 1970, "Aerodynamic Noise in Road Vehicles, Part 1: The Relationship Between Aerodynamic Noise and the Nature of the Airflow," The Motor Industry Research Association, p. 1971/2.
- [2] Thomson, J., 1964, "Wind Noise—A Practical Approach," Society of Automotive Engineers, Mar. 30–Apr. 3, p. 840B.
- [3] Stapleford, W., 1970, "Aerodynamic Noise in Road Vehicles, Part 2: A Study of the Sources and Significance of Aerodynamic Noise in Saloon Cars," The Motor Industry Research Association, p. 1972/6.
- [4] Watanabe, M., Harita, M., and Hayashi, E., 1978, "The Effect of Body Shapes on Wind Noise," Society of Automotive Engineers, p. 780266.
- [5] George, A., 1990, "Automobile Aerodynamic Noise," Society of Automotive Engineers, Feb. 26–Mar. 2, p. 900315.
- [6] Krajnović, S., and Davidson, L., 2003, "Numerical Study of the Flow Around the Bus-Shaped Body," *J. Fluids Eng.*, **125**, pp. 500–509.

- [7] Krajnović, S., and Davidson, L., 2005, "Flow Around a Simplified Car. Part I: Large Eddy Simulations," *J. Fluids Eng.*, **127**(5), pp. 907–918.
- [8] Krajnović, S., and Davidson, L., 2005, "Flow Around a Simplified Car. Part II: Understanding the Flow," *J. Fluids Eng.*, **127**(5), pp. 919–928.
- [9] Krajnović, S., 2002, Large-Eddy Simulations for Computing the Flow Around Vehicles, Ph.D. thesis, Chalmers University of Technology.
- [10] Rung, T., Eschricht, D., Yan, J., and Thiele, F., 2002, "Sound Radiation of the Vortex Flow Past a Generic Side Mirror," Eighth AIAA/CEAS Aeroacoustics Conference, Breckenridge, CO, Jun. 17–19, Paper No. AIAA-2002-2340.
- [11] Ffowcs Williams, J., and Hawkings, D., 1969, "Sound Generation by Turbulence and Surfaces in Arbitrary Motion," *Philos. Trans. R. Soc. London, Ser. A*, **264**(1151), pp. 321–342.
- [12] Posson, H., and Pérot, F., 2006, "Far-Field Evaluation of the Noise Radiated by a Side Mirror Using LES and Acoustic Analogy," 12th AIAA/CEAS Aeroacoustics Conference, Cambridge, MA, May 8–10, Paper No. AIAA-2006-2719.
- [13] Duncan, B., Sengupta, R., Mallick, S., Shock, R., and Sims-Williams, D., 2002, "Numerical Simulation and Spectral Analysis of Pressure Fluctuations in Vehicle Aerodynamic Noise Generation," SAE Paper No. 2002-01-0597.
- [14] Senthoran, S., Crouse, B., Noelting, S., Freed, D., Duncan, D., Balasubramanian, G., and Powell, R., 2006, "Prediction of Wall Pressure Fluctuations on an Automobile Side-Glass Using a Lattice-Boltzmann Method," AIAA/CEAS Aeroacoustics Conference and Exhibit, Cambridge, MA, May 8–10, Paper No. 2006-2559.
- [15] Gaylard, A., 2006, "CFD Simulation of Side Glass Surface Noise Spectra for a Bluff SUV," SAE Paper No. 2006-01-0137.
- [16] Curle, N., 1955, "The Influence of Solid Boundaries Upon Aerodynamic Sound," *Proc. R. Soc. London, Ser. A*, **A231**, pp. 505–514.
- [17] Ask, J., and Davidson, L., 2005, "An Acoustic Analogy Applied to the Laminar Upstream Flow Over an Open 2D Cavity," *C. R. Mec.*, **333**(9), pp. 660–665.
- [18] Ask, J., and Davidson, L., 2009, "Sound Generation and Radiation of an Open Two-Dimensional Cavity," *AIAA J.*, **47**, 1337–1349.
- [19] Larsson, J., 2002, "Computational Aero Acoustics for Vehicle Applications," Chalmers University of Technology.